Surface & Coatings Technology 470 (2023) 129811

Contents lists available at ScienceDirect

Surface & Coatings Technology

journal homepage: www.elsevier.com/locate/surfcoat

Residual elastic strain and survivability of stabilized zirconia coated carbon-carbon (C/C) composite

John I. Ferguson [a], Abdullah Al Saad [b], M. Hazar Seren [c,e], J.Y. Peter Ko [c], Kelly E. Nygren [c,d], Rodney W. Trice [b], Michael D. Sangid [a,b,*]

[a] School of Aeronautics and Astronautics, Purdue University, West Lafayette, IN 47907, USA
[b] School of Materials Engineering, Purdue University, West Lafayette, IN 47907, USA
[c] Materials Solutions Network at CHESS (MSN-C), Cornell University, Ithaca, NY 14853, USA
[d] Sibley School of Mechanical and Aerospace Engineering, Cornell University, Ithaca, NY 14853, USA
[e] ASML US, LP, Wilton, CT 06897, USA

ARTICLE INFO

Keywords:
Carbon-carbon
High energy X-ray diffraction
Residual stress
Energy-based modeling
Thermal protection system

ABSTRACT

Carbon-carbon (C/C) composites require protective coatings for prolonged use in elevated temperature, oxidizing environments. Ceramic coatings can provide oxidation protection; however, thermal expansion mismatch in conjunction with thermal events and interfacial constraint during coating deposition can result in residual stress, which can affect the lifetime and performance of the system. This work leveraged high energy synchrotron X-ray diffraction to determine the depth resolved residual elastic strain in two rare-earth oxide stabilized zirconia (12 mol% yttria and 6 mol% samaria) coatings, applied to a carbon-carbon composite substrate. The experimental characterization of the as-deposited coatings indicated a tension to compression residual elastic strain gradient, which was consistent with an energy-based model that illustrated the crystal structure dependence of the residual stress state. Via an oxyacetylene torch exposure, the ablation behavior and crack propagation were correlated to the measured residual elastic strain state and highlighted the influence of processing and exposure induced residual stress on coating performance. These experimental residual elastic strain measurements and relation to failure mechanisms support the survivability of these coating systems in applications that require thermal protection systems (TPS).

1. Introduction

Carbon fiber-reinforced carbon (C/C) composites are attractive candidates for high temperature structural materials (i.e., aircraft disc brakes, rocket nose cones, and nozzle components) due to low density, low thermal expansion, thermal stability, and strength and stiffness retention at elevated temperatures [1,2]. Additionally, the improved uniformity of properties in woven carbon fiber composites extends design opportunities [3]. However, the current employment of C/C composites as a high-temperature structural material is limited by the onset of volatile oxidation in air at temperatures greater than 500 °C [4,5]. For this reason, protective coatings are imperative to realize the benefits of C/C as a material candidate for elevated temperature applications.

Silicon carbide (SiC) is the historical coating solution for oxidation protection of C/C due to its good physical and chemical compatibility and formation of a dense, stable SiO_2 oxide layer up to 1500 °C [6]. With the current demands of hypersonic flight, a single phase SiC protective coating is not sufficient for operating windows above 1600 °C due to volatilization of the passive oxide to SiO gas [7,8] and below 1100 °C due to thermal expansion incompatibility induced cracking and debonding [9]. Recently, improved oxidation protection of C/C substrates has been achieved via multi-layer coatings with a ceramic oxidation protection coating [10–12], which generally provide advantageous fabricability over rare-earth silicate coating options [13]. For example, a $ZrSiO_4$ and aluminosilicate glass coating was shown to fill cracks in the SiC layer and protect the C/C substrate for continuous protection up to 1500 °C [10] and yttria stabilized zirconia (YSZ) based coatings, YSZ-La-Mo-Si [11] and SiC-YAG($Y_3Al_5O_{12}$)-YSZ [12], have effectively protected C/C from inward oxygen diffusion up to 1500 °C. Self-healing coatings such as these can retard crack growth; however, ultimately through thickness coating cracks degrade the protective

* Corresponding author at: School of Aeronautics and Astronautics, Purdue University, 701 W. Stadium Ave, West Lafayette, IN 47907, USA.
E-mail address: msangid@purdue.edu (M.D. Sangid).

https://doi.org/10.1016/j.surfcoat.2023.129811
Received 15 April 2023; Received in revised form 29 June 2023; Accepted 12 July 2023
Available online 14 July 2023

nature of these coatings and expose the underlying C/C substrate to rapid oxidation and failure.

While commonly listed as an origin of crack failure [7,8,10], residual stress due to deposition and thermal exposure has not been studied in plasma sprayed YSZ on C/C. Conversely, residual stress in YSZ coatings has been studied extensively for protection of metallic jet engine turbine blade materials. Several experimental neutron and X-ray diffraction (XRD) studies [14–17] have illustrated processing and exposure induced elastic strains as well as correlated failure mechanisms in YSZ coated Ni-based alloys. These studies include in-situ synchrotron XRD with applied load and temperature to illustrate the elastic strain gradient through the coating [14] and to identify the critical thermomechanical load state to induce cracking [15]. Additionally, ex-situ residual elastic strain characterizations reported depth-resolved residual elastic strains from quenching of molten spray particles and post-deposition cooling via synchrotron X-ray [16] and neutron diffraction [17] of YSZ coated metallic substrates. Lastly, analytical thin coating model efforts have identified the sensitivity of coating strain magnitudes and gradients to the mismatch in the coefficients of thermal expansion (CTE) [18] for YSZ coatings and correlated well to experimental relaxation due to micro-cracking [19].

As stated, crack formation resulting from quenching stress of sprayed YSZ molten particles [20] and stress upon cooling due to thermal expansion mismatch [19] between the C/C substrate and the coating can hinder oxidation protection. However, the current knowledge is limited to observational coating failure without quantification of the residual stress. In addition, studies on residual stress in YSZ coatings have not focused on application to woven C/C and the corresponding effects of weave geometry and reduced substrate CTE as compared with the often-studied metallic substrates. In this work, a 12 mol% yttria stabilized zirconia (YSZ) coating is leveraged as a baseline composition to compare with a 6 mol% samaria stabilized zirconia (SmSZ), C/C coating, with application temperatures up to 1800 °C [21]. Thus, the aim of this study is to quantify the residual stress state (via energy dispersive X-ray diffraction) of two stabilized zirconia coatings applied to C/C, then to understand this stress state in the context of the coating crystal structures, reinforced by a finite thickness coating model, and finally to leverage this characterization to inform and rationalize the coatings performance in representative thermal exposures (oxyacetylene torch).

2. Material and methods

2.1. Materials preparation

The substrate C/C panel, 5.5 mm thick, was commercially sourced (CeraMaterials, PA, USA). The C/C was formed from 12K Twill woven carbon fabric, that was impregnated with a carbon matrix and processed to 2000 °C, to achieve a composite density of 1.47 g/cm^3. C/C substrates were sectioned to 50 mm × 25 mm × 5.5 mm samples via a KBC Tools surface grinder with a diamond cutoff wheel. The substrate surfaces were then prepared for coating application by polishing with 320 grit SiC sandpaper followed by a 30 s pre-ablation exposure with an oxyacetylene torch. This pre-coating sample preparation produced surface channels, intended to form an interlocking transition layer between the substrate and coating. This transition layer has been shown to enhance adhesion strength and thermal shock resistance of C/C coatings [22], through a mechanism referred to as anchoring by Saad et al. [21]. Finally, the C/C substrates were ultrasonicated with a DI water and ethanol solution and dried in a muffle furnace at 135 °C for 2 h.

The SiC intermediary coating layer was applied via pack cementation as characterized by Hao et al. [23] with the following process: (a) the powder mixture consisting of 60 wt% Si (Aldrich Chemistry, 325 mesh, 99 % trace metals basis), 25 wt% C (Timrex KS6 Graphite, N-056), and 15 wt% Al_2O_3 (NanoTek Aluminium Oxide) was dry milled for 4 h with cylindrical alumina grinding media. (b) The prepared substrate C/C was embedded in the powder mixture in a graphite crucible. (c) Pack cementation was conducted in an argon atmosphere for 2 h at 1900 °C in a graphite heating element furnace (Carbolite LHTG 200–300/30-1G High-Temperature Furnace, Carbolite Gero Ltd, Derbyshire, UK). The resulting SiC layer was several microns thick (2.90 μm average), with a range of 2 μm to 5 μm along the surface of the C/C as verified by electron microscopy images and subsequent measurement via ImageJ.

The stabilized zirconia coatings were deposited via air-plasma spray deposition on the pack-cemented SiC layer bonded to the C/C substrate, as shown schematically in Fig. 1. Two varieties of zirconia coating were deposited and studied in this work: (a) 12 mol% Y_2O_3 stabilized ZrO_2 (YSZ) was commercially sourced (Praxair Surface Technologies #AI-1066, IN, USA) and (b) 6 mol% Sm_2O_3 stabilized ZrO_2 (SmSZ) was developed in-house via spray drying (Arch Spray Drying Services Inc., Brunswick, Georgia, USA). Prior to plasma spray, the loose powders for both coatings were studied via electron microscopy images with subsequent ImageJ measurements to inspect both particle size and shape and to confirm general acceptability, spherical powder with 10s of μm mean diameter, for plasma deposition. From this, the loose powder, pre-deposition, average particle size was 58 μm with a standard deviation of 10 μm for the YSZ powder, and average of 27 μm with a standard deviation of 19 μm for the SmSZ powder. The YSZ coating composition was selected as a baseline material due to its excellent thermal stability as a coating and prior use and study in gas-turbine engine applications to intermediate temperatures (approx. 1200 °C) [24] as well as potential as a constituent in composite coatings with applications over 2000 °C [25], while the SmSZ composition was studied with the goal of improved coating emissivity [26,27] and ablation resistance [28] up to higher service temperatures (1800 °C) [21]. For plasma spray deposition, the C/C substrates with the SiC intermediary layer were fixtured perpendicular to the plasma plume and preheated to 800 °C via a heat gun to reduce thermal shock from the aggressive plume heating and associated temperature gradient. The zirconia coatings were sprayed with the parameters listed in Table 1 to a nominal thickness of 150 μm (Metal Technology of Indiana Inc., IN, USA). During deposition, the plasma plume achieves temperatures of 8000–10,000 °C [29], which heats the deposited coating and substrate to a temperature of approximately 1000 °C [30] prior to the system cooling to room temperature. This processing-induced thermal event is a primary contributor to residual stress. After deposition, each sample was sectioned along the mid-length to 25 mm × 25 mm × ~5.65 mm via a surface grinder with a diamond cutoff wheel.

To simulate an in-use environment and to study survivability of the coating system, a single YSZ/SiC coated C/C sample was exposed to an oxyacetylene torch in accordance with ASTM E285-08 (2020). The sample was mounted in a graphite holder at a working distance of 50 mm from the torch tip to produce a heat flux of approximately 1.7 MW/m^2, as measured by a Thermogage TG-1000 (Vatell Corporation, VA, USA). The exposure was conducted for 60 s at a flame-facing surface temperature of approximately 1200 °C, as measured by a one-color

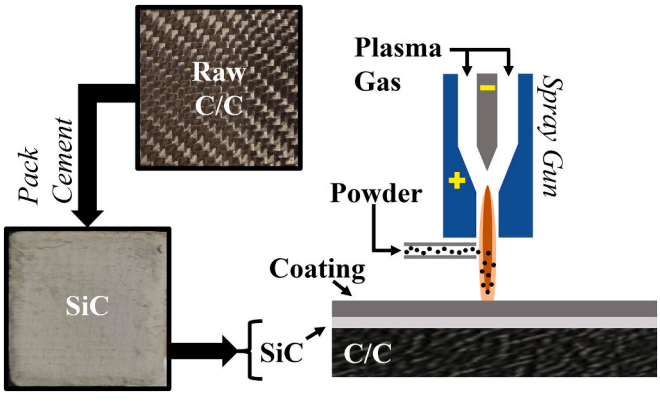

Fig. 1. Schematic (not to scale) of sample coating process.

Table 1
Plasma spray parameters used in zirconia coating application.

Parameter	Unit	Value
Primary gas, Ar	L/min	90
Secondary gas, H_2	L/min	2–6
Current	A	480
Voltage	V	65–70
Power	kW	31.2–33.6
Spray distance	mm	100
Powder feed rate	lb/h	5
Spray passes	–	4

pyrometer (OS3750, Omega Engineering Inc., Stamford, CT, USA) centered on the exposed sample surface and confirmed via a back surface Type S thermocouple measurement. A default emissivity value of 0.9 was used to determine the sample surface temperature by the pyrometer, because the exact coating emissivity at the applied temperature was not known. However, the actual emissivity of the YSZ coating surface at elevated temperatures was likely less than 0.9, such that the reported temperature reading of 1200 °C is lower than the actual sample surface temperature during exposure. The torch was operated with an oxidizing atmosphere via oxygen and acetylene flow rates of 12 slpm and 10 slpm, respectively. Ultimately, the as-deposited samples and exposed sample were cross-sectioned with a surface grinder to a size of 10 mm × 10 mm for microstructural characterization and energy dispersive X-ray diffraction (EDD) strain measurements. These final sectioning planes were along the outside square of the samples (not the coating face) such that there was minimal influence on the coating or residual stress measurements. Furthermore, the diamond cutoff wheel used to section samples for characterization is expected to have a maximum of a 0.1 mm affected zone [31], which is negligible compared with the 10 mm × 10 mm × 5.65 mm sample size. The three sample conditions studied in this work were an as-deposited 12 mol% YSZ/SiC coated C/C (YSZ-Dep), a post-deposition, oxyacetylene torch exposed 12 mol% YSZ/SiC coated C/C (YSZ-Exp), and an as-deposited 6 mol% SmSZ/SiC coated C/C (SmSZ-Dep). For ablation performance of the SmSZ/SiC coating applied to C/C, readers are directed to the work by Saad et al. [21].

2.2. Microstructural characterization

Complementary microstructural characterization to the EDD residual elastic strain measurements was conducted on the coating surface and cross-sectional views to understand the coating morphology and compositions. For cross-section characterization, samples were mounted in a resin such that the coating surface was preserved and then mechanically polished with a 1 μm diamond paste. Scanning electron microscopy (SEM) was conducted in an FEI Nova NanoSEM with an installed Oxford INCA Energy 250 system for elemental mapping via energy dispersive spectroscopy (EDS) and a Gaseous Analytical Detector (GAD) for backscatter electron (BSE) imagery. To determine the crystal structures of the stabilized zirconia coatings, conventional X-ray powder diffraction (XRD) was employed on the sample surfaces via a PANalytical Empyrean Powder X-ray Diffractometer with an X-ray generator input of 40 mA and 45 kV, a 0.08 s/step scan rate, a 0.03° step size, and a 20° to 80° scattering angle (2θ) range.

The coating surface topology was mapped via a Zygo ZeGage Pro optical profilometer. The full coating surface of each sample was measured with a 2.75× magnification objective lens, at a 3 μm lateral resolution. Post-processing of raw topology data and determination of surface roughness statistics were conducted in the Zygo Mx software.

2.3. Synchrotron X-ray characterization

Elastic strain measurements were performed on the Structural Materials Beamline (SMB) at the Cornell High Energy Synchrotron Source (CHESS). Energy dispersive X-ray diffraction (EDD), while commonly used for determining spatial fields of residual elastic strain at the component length scale, was selected as the experimental mode due to the high atomic number of the zirconia-based coatings, requiring high energies for X-ray transmission, and ideally to identify the residual elastic strain of each phase in a single region, simultaneously, by post-processing the diffraction peak profiles corresponding to each crystal structure. Additionally, the high brilliance synchrotron radiation, several orders of magnitude greater than conventional X-ray tube sources, allowed the measurement of bulk elastic strains at an increased resolution and confidence than traditional $\sin^2\psi$ methods.

The EDD setup consisted of a polychromatic X-ray source (50–200 keV) and a single-element Canberra GL-0055 energy-resolved detector positioned downstream of the sample at a horizontal takeoff angle (2θ) of 6.47317°. The EDD technique employs a transmission mode of X-ray diffraction, with a schematic illustration of the sample configuration shown in Fig. 2a. The diffraction volume, or sampling region, was defined by both the beam-defining slit (0.450 mm width by 0.015 mm height) and the downstream detector slits (0.450 mm width by 1.000 mm height) to produce a diffraction volume lozenge of 0.450 mm in the transverse direction (1-axis), 7.96 mm along the incident beam direction (2-axis), and 0.015 mm in the out-of-plane direction (3-axis). This elongated sampling region was selected to maximize the depth resolution of residual elastic strain to 0.015 mm, while maintaining a sufficiently large sampling region to reduce scan dwell times. Fig. 2b shows the position of the sampling region centroid (z_s) of the line scans, centered laterally within each sample, along the out-of-plane direction (3-axis). The line scans were conducted at 15 μm steps, from the first indication of the coating diffracted spectra until the diffraction peaks corresponding to the coatings were no longer apparent, followed by several 100 μm steps to probe the C/C substrate near the interface. The diffraction vector of this experiment, and thus the projected elastic strains, was in the 1–2 plane of Fig. 2a, which resulted in an in-plane residual elastic strain measurement, nearly aligned with the 2-axis.

The EDD data analysis was performed using a CHESS software package, consistent with analyses of previous studies [32] which was written in SciPy [33] using modules from HEXRD [34]. The diffracted spectra, as resolved on the downstream detector, are used to calculate elastic strain along specific lattice planes via Bragg's law. The true elastic strains, $\varepsilon_i^{el} = ln\left(\frac{d^i}{d_o^i}\right)$, for both coatings were calculated via the energy shift of the fitted diffraction peaks, simplified via Bragg's law for a single takeoff angle, as $\varepsilon_i^{el} = ln\left(\frac{E_o^i}{E^i}\right)$ [35], where d^i (Å) is the interatomic spacing for a specific (i^{th}) lattice plane of the phase in the stressed condition, and d_o^i (Å) is the corresponding stress-free spacing of the same lattice plane, while E^i (keV) is the diffracted energy peak of a specific (i^{th}) lattice plane of the phase as determined by the center of the Gaussian curve fit, and E_o^i (keV) is the corresponding stress-free energy of the same lattice plane. Thus, residual elastic strain (ε_i^{el}) was calculated along i lattice planes, maximum of 5 ($i = 1$ to 5), for each depth resolved scan through both the YSZ/SiC and SmSZ/SiC coated samples. The stress-free lattice parameter for the cubic YSZ, determined by EDD of the original loose powder at CHESS, was $a_{YSZ} = 5.1575$ Å. In addition, EDD of the loose SmSZ powder identified a stress-free lattice parameter of the tetragonal SmSZ of $a_{SmSZ} = 5.1440$ Å and $c_{SmSZ} = 5.1507$ Å, with a tetragonality (c/a) ratio of 1.0013.

3. Finite thickness coating model

3.1. Model formulation

An approach proposed by Stoney [36] and modified by Freund et al. [37] for finite thickness films is leveraged to understand the stress state that arises from the elastic incompatibility between the substrate C/C and coating: yttria stabilized zirconia (YSZ) and samaria stabilized

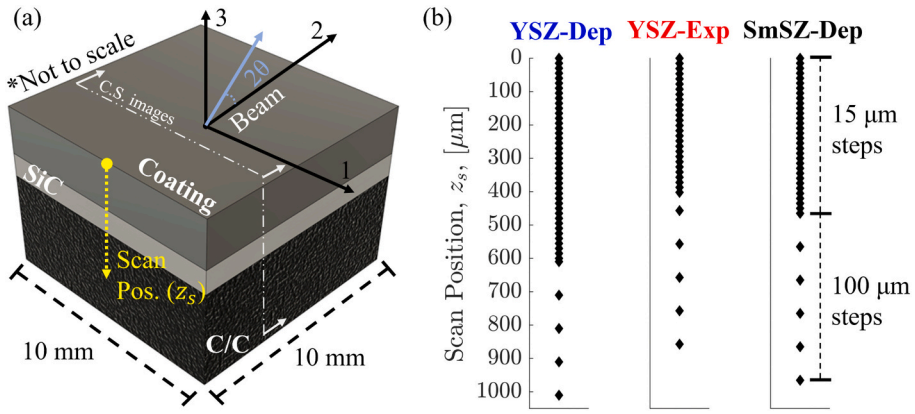

Fig. 2. (a) Schematic (not to scale) illustration of the EDD experimental setup and coordinates. (b) Beam centroid positions in the out-of-plane direction (3-axis), for scans through the depth of the sample for the as-deposited YSZ/SiC coating (YSZ-Dep), the torch-exposed YSZ/SiC coating (YSZ-Exp), and the as-deposited SmSZ/SiC coating (SmSZ-Dep).

zirconia (SmSZ) during cooling of the system after plasma spray deposition. The stabilized-zirconia coatings have a higher coefficient of thermal expansion (CTE) than the substrate C/C; thus, during cooling the coating is constrained at the interface and strains accrue in both materials. The thin, 2.90 μm average thickness, SiC intermediary layer is assumed to have a negligible impact on the elastic and expansion properties of the interface, and thus the system is modeled as two-phase with C/C as the substrate and YSZ or SmSZ as the coating. This approach assumes a perfect elastic bond upon completion of the coating spray deposition, followed by a constant uniform cooling of the entire system to room temperature.

During cooling, in the absence of externally applied stresses, the coating undergoes a state of biaxial stress. This stress is induced by the uniform strain due to the mismatch in thermal expansion coefficients of the substrate (α_s) and coating (α_c) as seen in Eq. (1).

$$\varepsilon_m = (\alpha_s - \alpha_c)\Delta T \tag{1}$$

To simulate cooling from plasma spray deposition, the modeled temperature change (ΔT) was −1000 °C [30]. To equilibrate the mismatch strain (ε_m), the coating and substrate are subject to a constant mid-plane extensional strain (ε_o) and curvature (κ) throughout the system [38]. Assuming both materials are isotropic, elastic, and homogenous, the expressions for the total strain (ε_s) through the thickness (h_s) of the substrate and the total strain (ε_c) through the thickness (h_c) of the coating, along the depth (z) of the system, are provided in Eqs. (2a) and (2b).

$$\varepsilon_s(z) = \varepsilon_o - \kappa z \quad \text{for} \quad -\frac{1}{2}h_s < z < \frac{1}{2}h_s \tag{2a}$$

$$\varepsilon_c(z) = \varepsilon_o - \kappa z + \varepsilon_m \quad \text{for} \quad \frac{1}{2}h_s < z < \frac{1}{2}h_s + h_c \tag{2b}$$

Thus, by leveraging the biaxial stress state of the coating, the strain energy density (U) through the depth of the coating is given by Eq. (3).

$$U(z) = \frac{E_c}{1-\nu_c}(\varepsilon_o - \kappa z + \varepsilon_m)^2 \quad \text{for} \quad \frac{1}{2}h_s < z < \frac{1}{2}h_s + h_c \tag{3}$$

where E_c and ν_c are the elastic modulus and Poisson ratio of the coating. From this, the strain in the coating is comprised of the constant mid-plane extensional strain (ε_o), the strain due to the constant curvature (κ) about the center of curvature, and the strain due to the mismatch in thermal expansion coefficients of the coating and substrate (ε_m).

As established by Saeidpourazar et al. [39], the mid-plane extensional strain (ε_o) and the curvature (κ) of the coating are solved by integrating the strain energy density (U) in Eq. (3) with respect to the thickness of the substrate and coating to find the potential energy (V), taking the variants, and confirming the stability of the system ($\partial V/\partial \varepsilon_o = 0$ and $\partial V/\partial \kappa = 0$). The resulting relationships are listed in Eqs. (4a) and (4b).

$$\kappa = \frac{\kappa_{st}(1+h)}{1+4hm+6h^2m+4h^3m+h^4m^2} \tag{4a}$$

$$\varepsilon_o = \frac{\varepsilon_{st}\left(1+h^3m\right)}{1+4hm+6h^2m+4h^3m+h^4m^2} \tag{4b}$$

where $\kappa_{st} = (6\varepsilon_m/h_s)hm$ and $\varepsilon_{st} = -\varepsilon_m hm$. The notation of h ($= h_c/h_s$) and m ($= E_c(1-\nu_s)/E_s(1-\nu_c)$) are the ratios of the coating to the substrate thicknesses and biaxial moduli, respectively. This formulation can be used to determine the stress in the coating and substrate; however, in this analysis, the curvature (κ) and potential energy (V) were the metrics selected to compare to the experimental residual elastic strain states of the two stabilized-zirconia coating systems.

3.2. Material properties

The finite thickness model approach requires elastic and geometric property inputs for both the substrate and coating materials. For both phases, the properties were assumed constant at their respective room temperature values due to the temperature insensitivity of these materials below 1000 °C. Additionally, the properties of the substrate were assumed to be purely dependent upon the C/C, neglecting the thin SiC intermediary layer. The material parameters required for the model are α, E, ν, h. Each material parameter model input was sourced from either literature (α, E, and ν) or from microscopy images of the samples (h), such that, the model implementation and experimental elastic strain measurements are independent. The values used for these parameters are listed in Table 2 and the determination of each parameter value is described in the forthcoming paragraphs.

The modeled substrate C/C thickness (h_s), as commercially sourced and measured, was 5.5 mm. The elastic and thermal properties of the modeled substrate were determined from woven carbon fiber literature values, as the carbon fibers govern the substrate and interface behavior.

Table 2
Mechanical and geometric parameters used in the finite thickness coating model for each material system: carbon-carbon (C/C), yttria stabilized zirconia (YSZ), and samaria stabilized zirconia (SmSZ).

Input model parameter	Unit	C/C	YSZ	SmSZ
CTE, α	ppm/°C	1.0	12.6–13.0	10.7–11.2
Young's modulus, E	GPa	300	36–42	33–39
Poisson ratio, ν	–	0.26	0.30	0.30
Thickness, h	mm	5.50	0.12–0.16	0.12–0.16

Furthermore, the in-plane woven morphology of the carbon fibers results in the macro-scale substrate properties to be primarily dependent on the longitudinal fiber properties. Therefore, the C/C is modeled as transversely isotropic, based on parameters measured parallel to the fibers. The modeled elastic modulus (E_s) was 300 GPa [40], Poisson ratio (ν_s) was 0.26 [41], and CTE (α_s) was 1.0 ppm/°C [42], in which the model uses the in-plane properties of the C/C material. These values are maintained the same for the modeling of both zirconia-based coatings.

The modeled coating (YSZ and SmSZ) property values were determined from literature based upon the experimentally observed crystallinity of the as-deposited coatings. As predicted for the respective stabilizing phase fractions, the YSZ (12 mol% yttria) coating was cubic and the SmSZ (6 mol% samaria) coating was tetragonal as determined by both EDD and conventional X-ray diffraction of the as-deposited samples. This variation in crystal structure necessitated independent elastic moduli (E_c^{YSZ} and E_c^{SmSZ}) and coefficients of thermal expansion (α_c^{YSZ} and α_c^{SmSZ}) for each coating. The nominal material parameters from literature were based on sintered sample properties, under the assumption that the yttria and samaria stabilized zirconia exhibit the same mechanical behavior, for a give phase fraction and crystal structure, due to the similar stoichiometry of the stabilizers. From this, the room temperature nominal sintered value of the CTE and elastic modulus for the tetragonal SmSZ were 10.7 ppm/°C [43] and 257 GPa [44,45], and for the cubic YSZ were 12.6 ppm/°C [46] and 277 GPa [45], respectively. In addition, from cross-sectional SEM evidence of both as-deposited samples, the nominal coating thickness (h_c^{YSZ} and h_c^{SmSZ}) was 0.15 mm, with a 0.12 mm minimum, 0.16 mm maximum, and 0.012 mm standard deviation. The isotropic Poisson ratio (ν_c^{YSZ} and ν_c^{SmSZ}) of stabilized zirconia is insensitive to crystal structure, and thus was modeled as 0.3 for both coatings [47]. Ultimately, the crystal structure dependent elastic and expansion properties of the stabilized-zirconia coatings were input into the energy-based finite thickness coating model to understand the variation in the experimental residual elastic strain metrics, based on crystallinity.

There is inherent uncertainty in material properties, which is especially exacerbated by the variability of molten particle impingement and cooling from plasma spray deposition. For this reason, a range of input parameters were modeled for both the YSZ and SmSZ coating properties. The observed coating thickness (h_c^{YSZ} and h_c^{SmSZ}) was nominally 0.15 mm; however, cross sectional microscopy indicated a range of 0.12 to 0.16 mm, as attributed to irregular passes and powder distribution during plasma-spray. In addition, the literature indicated a range of values for the CTE and the elastic moduli of both materials. The cubic YSZ coating CTE (α_c^{YSZ}) ranged from 12.6 ppm/°C [46] to 13.0 ppm/°C [48], while the tetragonal SmSZ coating CTE (α_c^{SmSZ}) ranged from 10.7 ppm/°C [43] to 11.2 ppm/°C [46]. These values for CTE of the tetragonal SmSZ coating were modeled as isotropic, without consideration of the asymmetry in the *a* and *c* crystal axes, due to the polycrystalline nature of the plasma-sprayed coating and the measured tetragonality ratio of nearly unity. The nominal elastic moduli of fully dense, sintered cubic (YSZ) and tetragonal (SmSZ) stabilized zirconia were 277 GPa and 257 GPa [44,45], respectively; however, previous studies [49,50] have highlighted the sensitivity of elastic moduli of these plasma-spray coatings to porosity. Few indications of porosity were seen in either as-deposited sample (YSZ-Dep and SmSZ-Dep) cross-sectional SEM micrographs; however, an independent study of coating porosity was outside the scope of this work. Therefore, to account for the potential debit in stiffness and to coincide with previous plasma-spray coating stiffness studies [51,52], the YSZ coating elastic modulus (E_c^{YSZ}) was modeled with a range of 36 to 42 GPa, while the SmSZ coating elastic modulus (E_c^{SmSZ}) was modeled from 33 to 39 GPa. These ranges were determined by debiting the sintered material literature values due to the nature of plasma-spray coatings, while maintaining the same parameter ratio due to crystallinity. The full list of model input parameters is summarized in Table 2. The range of values for each coating property propagated through the model to a range of modeled coating curvature (κ), Eq. (4a), and potential energy (V), the integration of strain energy density (U), Eq. (3), for each composition cooling to room temperature, post plasma spray deposition. These ranges are ultimately considered model uncertainty for comparison to the experimental residual elastic strain state of both coatings.

3.3. Coating stress state metrics

The goal of the finite thickness coating model was to compare with the residual elastic strain state, determined via the experimental EDD measurements. Specifically, to investigate the effect of coating crystallinity on the residual stress formation in plasma spray zirconia coatings. To achieve an equitable comparison, the model and experimental results are maintained wholly independent via the model input parameters from literature, with no corroboration with the experiment prior to the metrics described in this section.

The first stress state metric leveraged to compare between the model and experiment is based on the curvature induced by the equilibrating of the mismatch stress upon cooling from plasma spray deposition. The constant curvature (κ) in the model formulation, Eq. (4a), is the only contributor to the variation in depth-resolved elastic strain in the coating (ε_c), shown via the differentiation of Eq. (2b), $\frac{\partial \varepsilon_c}{\partial z} \left(= -\kappa \right)$. For this reason, the model curvature is compared with the residual elastic strain gradient (m), or slope, as determined via a linear curve fit of the experimental elastic strain results (ε^{el}) through the coating depth. For the comparison between the two coating compositions, the tetragonal SmSZ and the cubic YSZ, the model (κ) and experiment (m) metrics are implemented as ratios, with the description, $\Theta \left(= \frac{\kappa_{SmSZ-Dep}}{\kappa_{YSZ-Dep}} \right)$ and $\beta \left(= \frac{m_{SmSZ-Dep}}{m_{YSZ-Dep}} \right)$. Thus, the curvature-based relation is the comparison of the Θ ratio from the model, accounting for input parameter uncertainty, to the β ratio from the experiment. As this comparison is based upon ratio values between the two coatings, the negative sign in the differentiation of Eq. (2b) is cancelled.

In addition, an energy metric was leveraged to further substantiate the comparison between the model results and experiment. The model is primarily an energy formulation such that the strain terms are determined via the potential energy of the coating (V), found via the integration of the elastic strain energy density (U), in Eq. (3), over the coating depth. This model potential energy (V) represents the total strain energy in the coating, and as such is compared with the total residual elastic strain energy density, $W \left(= \int U^{el} dz = \int \frac{1}{2} E \left(\varepsilon^{el} \right)^2 dz \right)$, as determined via the discrete integration of the experimental strain energy density (U^{el}) over the coating depth. As in the curvature comparison, for the tetragonal SmSZ and the cubic YSZ, the model (V) and experiment (W) metrics are implemented as ratios, with the description, $\Phi \left(= \frac{V_{SmSZ-Dep}}{V_{YSZ-Dep}} \right)$ and $\Psi \left(= \frac{W_{SmSZ-Dep}}{W_{YSZ-Dep}} \right)$. Thus, the energy-based relation was the comparison of the Φ ratio from the model, accounting for input parameter uncertainty, to the Ψ ratio from the experiment.

The combination of these two metrics is leveraged in this work to provide rationale for the variation in stress state between the two stabilized zirconia coatings, which ultimately impacts the performance and survivability of each composition.

4. Results and discussion

4.1. Structure and composition of coatings

A micrograph of the as-deposited SmSZ/SiC coated C/C (SmSZ-Dep) sample cross-section without polish is illustrated in Fig. 3. Note, the as-deposited YSZ/SiC coating illustrated a consistent morphology as shown

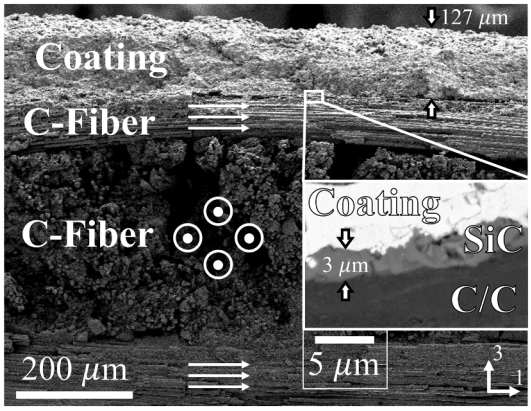

Fig. 3. Cross-sectional SEM images of the as-deposited SmSZ/SiC (SmSZ-Dep) coated C/C with arrows to indicate the carbon fiber (C-Fiber) directions and to notate the layer thicknesses.

in the polished condition in Fig. 7a. The inlay, backscatter electron (BSE) image, magnifying the C/C-SiC-Coating interfaces illustrated that the pack cementation and plasma spray deposition resulted in no interfacial voids and intact bonding between each coating layer. The SiC layer, seen in the inlay BSE image as the grey middle layer, had a thickness range of 2 μm to 5 μm across the cross-section, with little porosity and observable penetration between carbon fiber tows from the pack cementation process. This penetration of the SiC layer between the carbon fiber tows caused the variation in thickness of the layer. Furthermore, the penetration of the SiC and YSZ/SmSZ coating into the fiber tows has been shown to be beneficial to coating survivability due to improved adhesion strength via mechanical anchoring [21,53]. The expected thickness from plasma spray deposition of a nominal 150 μm coating (for both YSZ and SmSZ coatings) was achieved. However, due to the variability in the molten particles used in the plasma spray process, the YSZ and SmSZ coatings illustrated a range in thickness from 120 μm to 160 μm. Additionally, the top surface, as seen in Fig. 3, qualitatively illustrates surface roughness that resulted from plasma spray application.

The samaria stabilized zirconia (SmSZ) coating was studied for its potential increased emissivity and comparable thermal stability compared to the baseline YSZ coating. SEM images, as well as EDS elemental maps of the SmSZ sample surface were conducted to confirm deposition quality as shown in Fig. 4. The surface shown in the SEM image indicated an even application with regions of fully fused coating layers as well as interspersed voids, due to variability in the feedstock

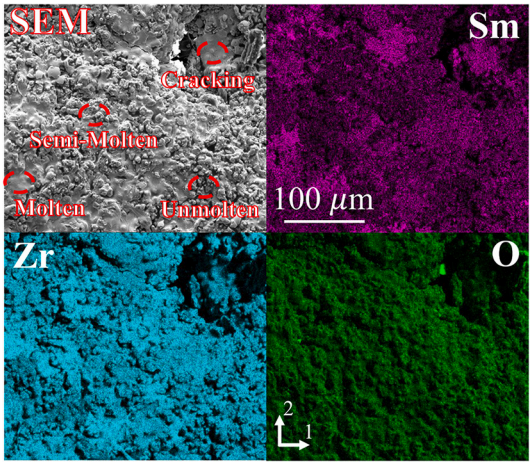

Fig. 4. Surface morphology from SEM image and qualitative composition (EDS elemental maps) of the as-deposited SmSZ/SiC (SmSZ-Dep) coated C/C with circles and labels to indicate representative plasma spray deposition features.

particle size and splat behavior of molten, semi-molten, and unmolten particles in the plasma-spray deposition process [54]. In addition, microcracking was seen within the fully fused regions, which is characteristic of plasma-sprayed ceramic coatings, due to contraction upon cooling, which induces tensile quenching stress [55]. However, void formation and microcracking were expected in the coating deposition process and are not necessarily indicative of poor coating performance. The EDS composition maps showed even dispersion of the SmSZ coating constituent elements, which confirmed the composition of the original powders and the suitability of this coating system for plasma spray application.

The crystal structure of the zirconia coatings is of importance for both the stability of the phase during thermal exposure, as well as for accurately determining the residual elastic strains in the EDD measurement. XRD was conducted to verify the crystal structures of each sample, as seen in Fig. 5. As expected for the 12 mol% stabilizing phase fraction of yttria, the YSZ coating illustrated a cubic crystal structure (PDF Card 04–022-7386). In addition, the comparison of the YSZ-Dep and YSZ-Exp XRD patterns indicated that no phase change occurred during the oxyacetylene torch exposure, which reinforced the thermal stability of YSZ as a coating. The peak doublets in the YSZ-Dep and YSZ-Exp spectra at the [4 0 0] lattice plane peak ($2\theta = 73.5°$), with the second peak at approximately half the intensity of the first, is characteristic of the X-ray peaks corresponding to the $K\alpha_1$ and $K\alpha_2$ wavelengths spreading at higher scattering angles and not indicative of crystal tetragonality. However, the 6 mol% SmSZ coating illustrated a tetragonal crystal structure (PDF Card 04–019-6351) as shown by the splitting of the cubic [4 0 0] lattice plane peak into two equal intensity peaks corresponding to the [0 0 4] lattice plane ($2\theta = 73.3°$) and [4 0 0] lattice plane ($2\theta = 74.3°$) in Fig. 5. Additionally, the lower scattering angle peaks corresponding to the [0 2 0] lattice plane ($2\theta = 35.0°$) and the [1 3 1] lattice plane ($2\theta = 60.0°$) illustrated nearly equal intensity double peaks indicating the tetragonality the SmSZ coating crystal structure. The tetragonality (c/a) ratio was 1.0013, which indicated the 6 mol% Sm_2O_3 stabilized zirconia (SmSZ) coating stabilized as the non-transformable t′ zirconia crystal structure, which has been shown to be highly stable and durable during high-temperature exposures [56]. Finally, the low intensity peaks around the [1 1 1] peak ($2\theta = 28–33°$) indicated the presence of a small percentage of monoclinic phase in the as-deposited SmSZ coating. This monoclinic phase was a consequence of the reduced Sm_2O_3 phase fraction not fully stabilizing the SmSZ coating

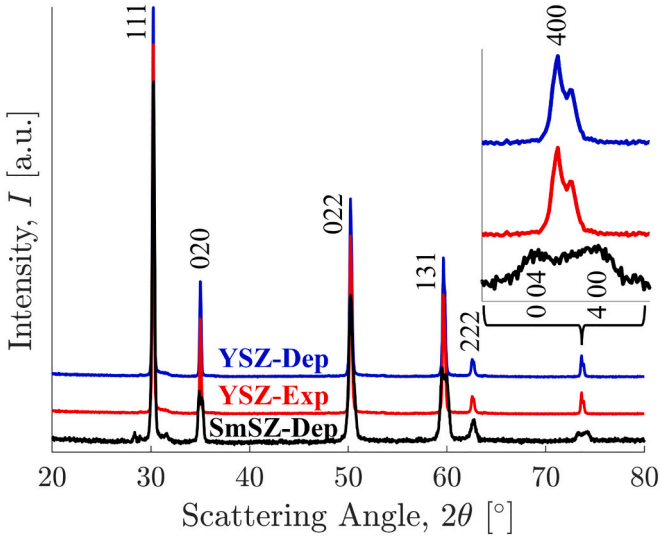

Fig. 5. XRD pattern of the as-deposited YSZ/SiC coating (YSZ-Dep: PDF Card 04-022-7386), the torch-exposed YSZ/SiC coating (YSZ-Exp: PDF Card 04-022-7386), and the as-deposited SmSZ/SiC coating (SmSZ-Dep: PDF Card 04-019-6351).

and was assumed negligible to the material properties and performance of the coating system due to the small percentage, 3.6 mol%, as calculated via the Toraya method [21].

4.2. Microstructural effects of torch exposure

The coating surface topology of each sample is shown in Fig. 6, where the surface height indicated by the colormap is aligned with the 3-axis in Fig. 2a. The statistics over the entire coating surfaces showed that the root mean square height (S_q) for the YSZ-Dep, the YSZ-Exp, and the SmSZ-Dep samples was 26.3 μm, 41.2 μm, and 47.7 μm, respectively. The increase in S_q of the torch exposed YSZ sample (YSZ-Exp) as compared to the as-deposited YSZ sample (YSZ-Dep) was due to ablation and the associated inconsistent material loss during exposure. The SmSZ coating had the largest root mean square height and the surface topology, seen in Fig. 6c, illustrated the most detailed depiction of the underlying woven C/C fiber tows. These results are hypothesized to be a consequence of increased penetration of the SmSZ powders between surface tows of the C/C substrate due to the reduced size and more irregular distribution of the original SmSZ powder, developed via spray drying. The average particle sizes were 58 μm with a standard deviation of 10 μm for the YSZ powder, and average of 27 μm with a standard deviation of 19 μm for the SmSZ powder. This penetration between individual fiber tows is beneficial to the survivability of the coating due to mechanical anchoring with the substrate, which improves adhesion strength and reinforces the coating-substrate interface against spallation or exfoliation.

The polished cross-sections of the as-deposited YSZ coating sample (YSZ-Dep) and the post-torch exposure sample (YSZ-Exp) are shown in Fig. 7. However, at this magnification, the SiC intermediate layer was not apparent. The YSZ-Dep sample, Fig. 7a, showed no indications of transverse crack growth from plasma spray deposition or associated cooling. This crack-free as-deposited sample indicated that the elastic mismatch strain from the incompatible thermal expansion coefficients of the substrate C/C and YSZ coating did not approach the stress to induce coating failure. This reinforced the potential of a YSZ coating for protection of the C/C substrates. In addition, the absence of crack formation from deposition cooling supported the model comparison, which assumed a homogenous coating layer. The pre- and post-exposure mass measurements of the YSZ-Exp sample indicated a mass loss due to ablation that was equivalent to a 60 μm thickness loss. Additionally, the post-torch exposed (YSZ-Exp) sample, Fig. 7b, showed significant crack networks near the free surface, due to the stress fields resulting from the mismatch in thermal expansion coefficients and subsequent ablation. Through-thickness cracks in the coating in Fig. 7b traversed from the free surface to approximately the mid-depth of the coating, and in most instances did not extend to the C/C substrate. The measured depth of transverse cracks in the coating was approximately 50 μm, ranging from 46 μm to 60 μm in the cross-sectional images. The consolidation of significant crack networks only in the vicinity of the free surface, as well as the stunted crack growth prior to penetration of the substrate interface, indicated that the coating maintained its oxygen diffusion protection throughout the torch exposure and is another aspect that supports YSZ as a coating candidate for C/C.

4.3. Residual elastic strain of coatings

The full spectra, raw diffraction signal from the EDD scans through the depth of the coating and substrate for each sample are illustrated in Fig. 8. The thin SiC intermediate layer did not produce observable diffraction data because the limited material volume, 2 μm to 5 μm thickness, generated a diffracted signal that was below the noise of the detector. The SiC material volume was at the maximum only a fraction of the 15 μm diffracted region height, which due to the variability in the surface topology of the C/C substrate fiber tows, was likely never fully contained nor centered during the depth-resolved scans. Therefore, the

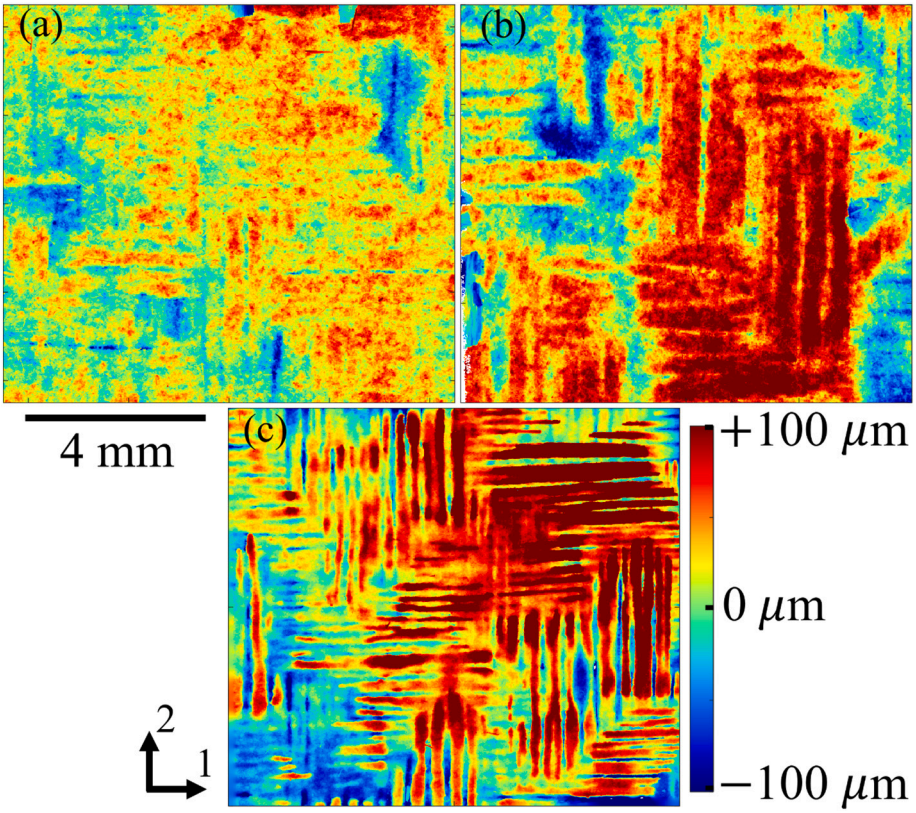

Fig. 6. Surface topology of (a) the as-deposited YSZ/SiC coating (YSZ-Dep), (b) the torch-exposed YSZ/SiC coating (YSZ-Exp), and (c) the as-deposited SmSZ/SiC coating (SmSZ-Dep).

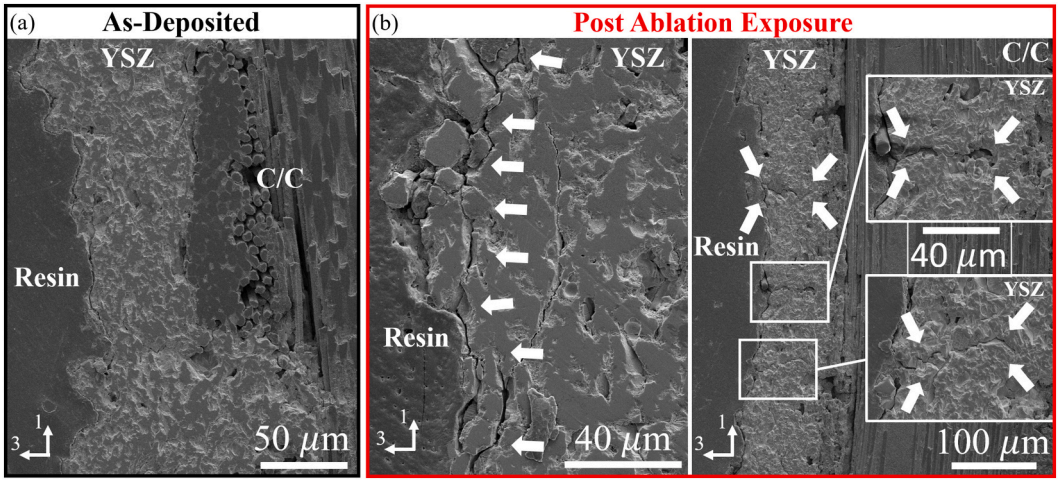

Fig. 7. SEM cross-sectional images of (a) the as-deposited YSZ/SiC coating (YSZ-Dep) and (b) the torch-exposed YSZ/SiC coating (YSZ-Exp) with arrows to indicate cracks.

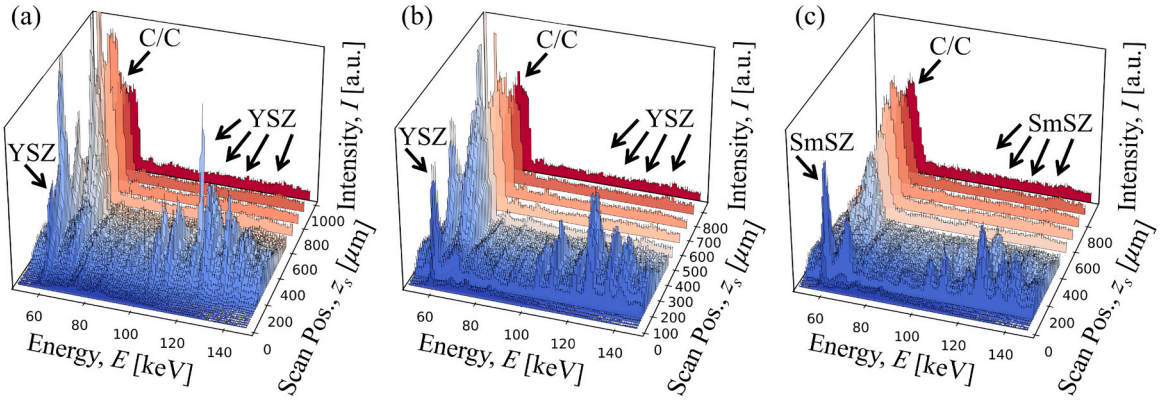

Fig. 8. Full spectra, raw diffraction signal for (a) the as-deposited YSZ/SiC coating (YSZ-Dep), (b) the torch-exposed YSZ/SiC coating (YSZ-Exp), and (c) the as-deposited SmSZ/SiC coating (SmSZ-Dep) with arrows to indicate the diffracted peaks of each phase.

SiC residual elastic strains were not reported. As seen in Fig. 8, the C/C substrate was probed for each sample and the diffraction spectra were measured; however, the hexagonal graphite-like fibers and matrix produced highly convoluted diffraction peaks, between 62 and 70 keV. The deconvolution of these peaks reduced the confidence in the Gaussian fit operation for elastic strain and thus strains for the C/C were not reported. For this reason, the residual elastic strains in the YSZ and SmSZ coatings are the focus of this work.

For each sample EDD measurement, first an X-ray transmission measurement scanned from above the free surface of the sample into the coating, 3-axis in Fig. 2a. A step function was fit to the reduction in flux, due to the absorption of the coating, to locate the presumed free surface and thus the initial scan position of the line scans shown in Fig. 2b. The surface roughness from the plasma spray deposition, illustrated in Fig. 6, resulted in the first several scans along the depth of each sample to exhibit low diffraction intensity, prior to the full 15 μm height of the diffraction volume, being contained within the sample. Therefore, the free surface and subsequently reported depth (z) in the experimental elastic strain measurements are in reference to the beam centroid position in the out of plane direction (z_s), where sufficient diffraction energy to conduct a least squares fit for elastic strain was achieved.

The elongated diffraction volume, 7.96 mm in the coating plane (2-axis in Fig. 2a), resulted in an increased perceived depth of the coatings in the EDD strain results. This was a result of variation in macroscale, out of plane (3-axis) features of the coating and substrate morphology over the nearly 8 mm in-plane length of the diffraction volume. For instance, topographical features such as the surface roughness, illustrated in Fig. 6, and the interface roughness, illustrated in Fig. 7, resulted in the fine 0.015 mm depth-wise diffraction volume height to illuminate coating volume for more scans along the 3-axis (z_s) than the coating thickness. Additionally, any tilt or macro-form of the C/C substrate compounded this effect, which resulted in diffraction peaks corresponding to both the YSZ and SmSZ coatings to appear in more depth-resolved scans than the nominal 0.15 mm nominal coating thickness. For these reasons, the EDD measurement depth (z) is reported for the full range of scans, in which the coating diffraction peaks were collected with enough intensity counts to fit a Gaussian curve and to determine an elastic strain value with confidence.

As previously mentioned, via conventional XRD and EDD scans of the loose powder YSZ and SmSZ coating materials, the crystal structures were determined to be cubic ($a_{YSZ} = 5.1575$ Å) and tetragonal ($a_{SmSZ} = 5.1440$ Å, $c_{SmSZ} = 5.1507$ Å), respectively. In addition, Fig. 5 shows that no phase change occurred in the YSZ upon deposition or exposure. Thus, as previously described, elastic strains were determined along individual lattice planes corresponding to the crystal structure of each material. A weighted-average metric was implemented to directly compare the residual elastic strain between each sample while accommodating for the variation in crystal structure [57]. The integrated intensity of each individual diffraction peak, corresponding to the elastic strain value along the specific lattice plane, was selected as the weight metric. This weight was chosen because in diffraction-based elastic strain measurements, the integrated intensity is indirectly correlated with strain uncertainty [58].

Therefore, this method prescribed an increased weight to the directly measured lattice plane strain values with increased experimental confidence. The elastic strains reported in Fig. 9 were determined via the equation $\varepsilon^{el} = \frac{\sum [Integrated\ Intensity]_i \varepsilon_i^{el}}{\sum [Integrated\ Intensity]_i}$, where the summation is conducted for i diffraction peaks for which the experimental elastic strain (ε_i^{el}) was determined along the corresponding (i^{th}) lattice plane. This residual elastic strain (ε^{el}) was calculated at each depth-resolved scan location for each sample, which resulted in a strain component along the diffraction vector, closely aligned with the sample 2-axis in Fig. 2a. The complementation of strain measurements across multiple lattice planes is another benefit of EDD in reducing uncertainty in the residual stress state.

The weighted-average, depth-resolved, residual elastic in-plane strain for each sample are displayed in Fig. 9. The as-deposited samples, YSZ-Dep and SmSZ-Dep, illustrated a tension to compression gradient from near the free surface towards the substrate C/C. From this, the maximum tensile elastic strain near the coating surface for the YSZ/SiC and SmSZ/SiC coating is 0.155 % and 0.164 %, respectively. This strain gradient is primarily a result of the elastic mismatch strain during cooling from plasma spray deposition, equilibrating with an induced curvature of the coating and substrate. This curvature relationship with residual elastic strain is the basis of the finite thickness coating biaxial stress model. Additionally, a primary benefit of the weighted elastic strain, reported in Fig. 9, is that it aligns well with the isotropic modeling formulation, which enabled comparison between the experimentally measured residual elastic strains and the model results. Note, the increased scatter in the SmSZ-Dep sample residual elastic strains was attributed to the increased penetration of the SmSZ powder into the carbon fiber tows during deposition and subsequently higher surface roughness indicated in Fig. 6c.

As previously mentioned, and illustrated in Fig. 6b, the YSZ-Exp sample coating surface was ablated by 60 μm during the oxyacetylene torch exposure. To account for the material loss and to allow for reasonable comparison to the as-deposited samples, the YSZ-Exp elastic strains in Fig. 9 were shifted by 60 μm in depth. The shifted YSZ-Exp residual elastic strain indicated that the ablation occurred in the tensile region of the as-deposited coating, which was rationalized by tensile residual stress near the free-surface amplifying the torch-induced expansion stress, which resulted in preferential ablation of this region. Additionally, the through-thickness crack growth that halted near the mid-depth of the coating in the YSZ-Exp sample, Fig. 7b, is likely a result of crack-arresting compressive residual elastic stress in the YSZ-Exp sample. The correlation of these results indicated that the ablation torch exposure relaxed the residual elastic strain gradient and the magnitude of compressive residual elastic strain near the C/C substrate interface in the YSZ-Exp sample as compared to the as-deposited YSZ-Dep sample and that the relaxation mechanism was transverse crack growth, as seen in the inset images in Fig. 7b. Overall, these findings highlighted the effect of residual stress from plasma-spray deposition on the failure mechanisms such as ablation and transverse crack growth, and ultimately the survivability of the YSZ coating system applied to C/C.

4.4. Finite thickness coating model comparison

The residual elastic strain state of the two as-deposited coating samples, YSZ-Dep and SmSZ-Dep are compared via two residual elastic strain metrics, shown in Fig. 10. As described in Section 3.3, these metrics were selected to compare to the finite thickness coating model and to rationalize the comparison with the variation in coating crystal structure. As previously mentioned, both the as-deposited samples (YSZ-Dep and SmSZ-Dep) developed a residual elastic strain gradient (m), during cooling from plasma-spray deposition. This gradient was determined via a linear fit as shown in Fig. 10a. From the fit, the elastic strain gradient for the YSZ-Dep ($m_{YSZ-Dep}$) and SmSZ-Dep ($m_{SmSZ-Dep}$) samples were −1.17e−3 and −8.79e−4 percent strain per micron, respectively. The resulting ratio between the SmSZ-Dep and the YSZ-Dep elastic strain gradient, defined as $\beta\ (= \frac{m_{SmSZ-Dep}}{m_{YSZ-Dep}})$, was 0.75. In addition, the total elastic strain energy density, $W\ \left(= \int U^{el} dz = \int \frac{1}{2} E \left(\varepsilon^{el}\right)^2 dz\right)$, illustrated in Fig. 10b, were 103.4 and 54.12 N/m for the YSZ-Dep ($W_{YSZ-Dep}$) and SmSZ-Dep ($W_{SmSZ-Dep}$) samples, respectively. The resulting ratio between the SmSZ-Dep and the YSZ-Dep total energy, defined as $\Psi\ (= \frac{W_{SmSZ-Dep}}{W_{YSZ-Dep}})$, was 0.52. For both these experimental elastic strain state metrics, $\beta = 0.75$ and $\Psi = 0.52$, the tetragonal SmSZ-Dep coating illustrated a reduced value compared to the cubic YSZ-Dep coating. To understand this trend, the ratio of experimental elastic strain gradients (β) and the ratio of experimental total elastic strain energies (Ψ) were compared to the results from the crystal structure dependent finite thickness coating model, as described in Section 3.3.

Previous works have shown that tetragonal stabilized zirconia (SmSZ) has a reduced CTE and elastic modulus compared to cubic stabilized zirconia (YSZ), as stated in Section 3.2. In addition, the coating elastic and expansion property value inputs to the model have inherently high uncertainty, due to the variability in coating porosity and molten particle splat layer geometry during plasma-spray deposition, as well as the property dependence on the phase fraction of the oxide stabilizer in these zirconia material systems. To incorporate this uncertainty in the model, the range of property values found in literature for

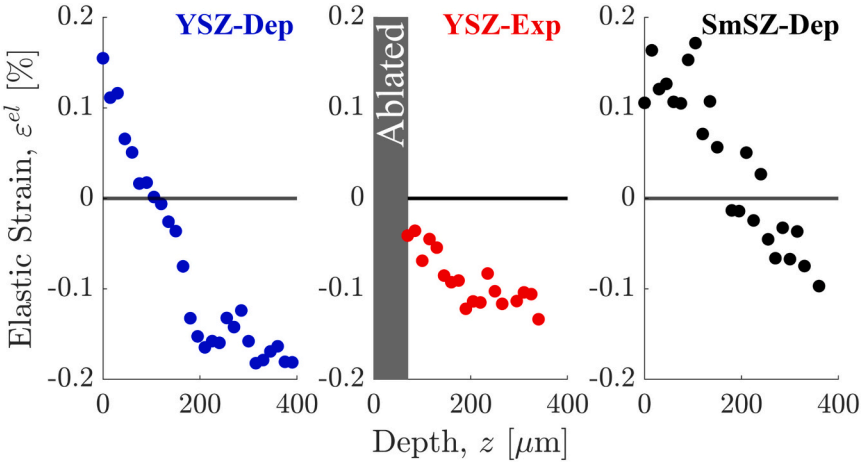

Fig. 9. Experimental in-plane, depth-resolved elastic strain for the as-deposited YSZ/SiC coating (YSZ-Dep), the torch-exposed YSZ/SiC coating (YSZ-Exp), and the as-deposited SmSZ/SiC coating (SmSZ-Dep).

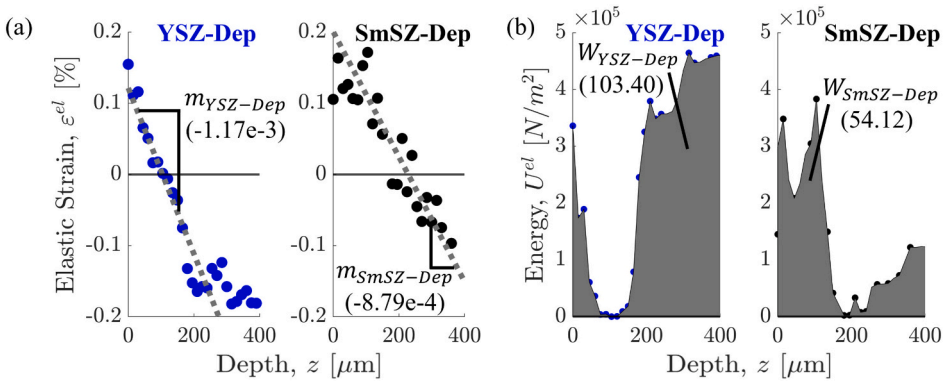

Fig. 10. Experimentally derived (a) gradient in elastic strain (m) and (b) total elastic strain energy density (W) for the as-deposited YSZ/SiC coating (YSZ-Dep) and the as-deposited SmSZ/SiC coating (SmSZ-Dep). The units for m and W are reported in [%/μm] and [N/m], respectively.

each coating composition, as listed in Table 2, were used to determine a range of ratios for each respective parameter – ratio of thickness (h_c^{SmSz}/h_c^{YSZ}), ratio of modulus (E_c^{SmSz}/E_c^{YSZ}), and ratio of CTE ($\alpha_c^{SmSz}/\alpha_c^{YSZ}$). Ultimately, this range of model input parameters propagated to a range of values for the model ratio of curvature (κ), defined as $\Theta\ (=\frac{\kappa_{SmSZ-Dep}}{\kappa_{YSZ-Dep}})$, as well as the ratio of model potential energy (V), defined as $\Phi\ (=\frac{V_{SmSZ-Dep}}{V_{YSZ-Dep}})$, between the SmSZ-Dep and YSZ-Dep coatings. The results for these model ratio metrics are illustrated in Figs. 11 and 12. In Figs. 11a and 12a, a 3D volume is generated from the three model input parameter ratios, with the color on the depicted 2D planes indicating the ratio of the model stress state metric, Θ in Fig. 11a and Φ in Fig. 12a. Additionally, for the nominal input parameter ratios from literature or experimental observations ($\frac{E_c^{SmSz}}{E_c^{YSZ}}=0.93$, $\frac{\alpha_c^{SmSz}}{\alpha_c^{YSZ}}=0.85$, and $\frac{h_c^{SmSz}}{h_c^{YSZ}}=1$) the model theoretical ratio of curvature, Θ^* in Fig. 11, and ratio of potential energy, Φ^* in Fig. 12 are indicated by black stars in the 3D volume as well as the color bar. These theoretical model ratio values are then compared with the corresponding stress metrics from the experimental residual elastic strain to deduce the effect of coating crystallinity on the residual stress state arising from plasma-spray deposition.

The volumetric map of the model curvature ratio, Eq. (4a), of the SmSZ coating to the YSZ coating (Θ), accounting for the range of values in the model inputs is shown in Fig. 11a. In addition, Fig. 11b is a two-dimensional view of the computed curvature ratio (Θ) with respect to the single CTE ratio of SmSZ to YSZ for the theoretical ratio of both thickness, 1, and elastic modulus, 0.93. As seen in Fig. 11, the theoretical ratio of curvature (Θ^*) from the model is 0.78, as calculated with the nominal ratio of all three input parameters of the tetragonal SmSZ to the cubic YSZ coatings. This model curvature ratio is found via differentiating the total strain in the coating, Eq. (2b), with respect to the z, $\frac{\partial\epsilon_c(z)}{\partial z}\ (=-\kappa)$, such that this metric is directly comparable to the elastic strain gradient ratio metric from the experiment. From this, the ratio of experimental elastic strain gradients (β), 0.75 in Fig. 10a, was consistent with the theoretical ratio of model curvature (Θ^*), 0.78. This result was one indication that the variation in experimental residual elastic strain between the SmSZ-Dep and YSZ-Dep samples is attributable to the difference in crystal structures.

Similarly, the volumetric map of the model potential energy ratio (Φ), the integration of Eq. (3) over the thickness of the coating, for the SmSZ coating to the YSZ coating, accounting for the range of values to each model input is shown in Fig. 12a, with Fig. 12b illustrating a two-dimensional view of the computed potential energy ratio (Φ) with respect to the single CTE ratio of SmSZ to YSZ for the theoretical ratio of both thickness, 1, and elastic modulus, 0.93. As seen in Fig. 12, the theoretical ratio of potential energy (Φ^*) from the model is 0.66, as calculated with the three nominal input parameters of the tetragonal SmSZ to the cubic YSZ coatings. This modeled total potential energy over the full coating thickness is directly comparable to the

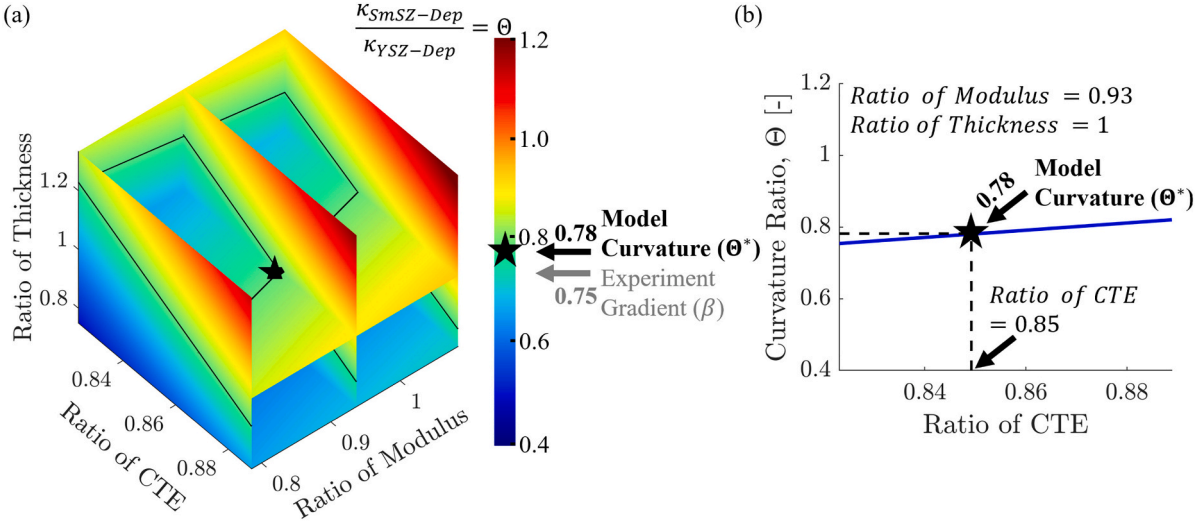

Fig. 11. Finite thickness coating model derived curvature ratio (Θ) of the as-deposited SmSZ/SiC coating ($\kappa_{SmSZ-Dep}$) to the as-deposited YSZ/SiC coating ($\kappa_{YSZ-Dep}$) for the model input value ratio of the tetragonal SmSZ to the cubic YSZ, accounting for uncertainty in (a) CTE (α_c), modulus (E_c), and thickness (h_c) and (b) CTE (α_c), with the theoretical ratios of thickness (1) and elastic modulus (0.93).

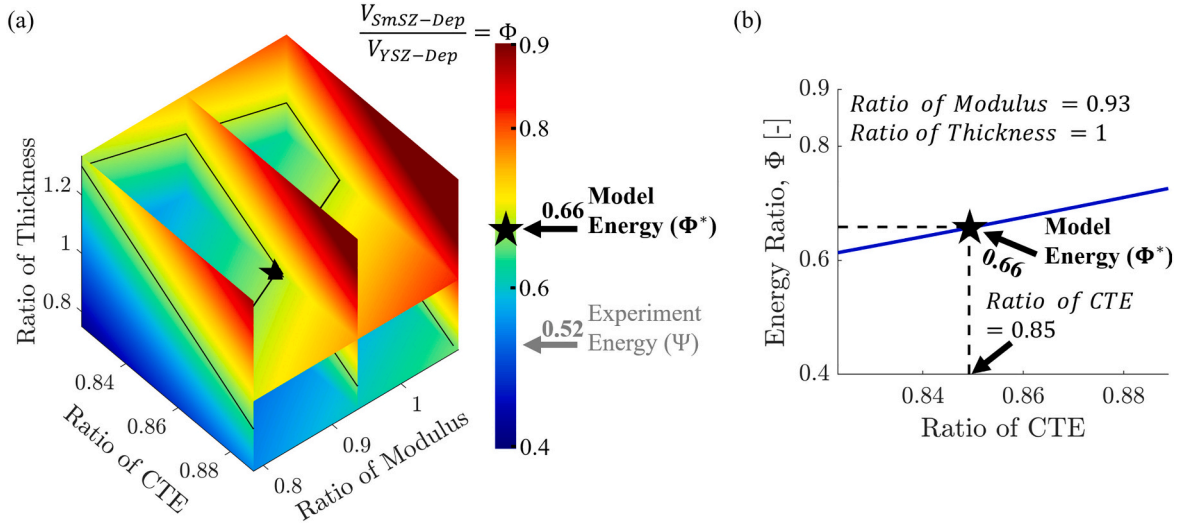

Fig. 12. Finite thickness coating model derived total strain energy density ratio (Φ) of the as-deposited SmSZ/SiC coating ($V_{SmSZ-Dep}$) to the as-deposited YSZ/SiC coating ($V_{YSZ-Dep}$) for the model input value ratio of the tetragonal SmSZ to the cubic YSZ, accounting for uncertainty in (a) CTE (α_c), modulus (E_c), and thickness (h_c) and (b) CTE (α_c), with the theoretical ratios of thickness (1) and elastic modulus (0.93).

experimental total elastic strain energy density. From this, the ratio of total elastic strain energy density from the experimental residual elastic strain (Ψ), 0.52 in Fig. 10b, was contained in the range of the model calculated potential energy ratios (Φ), based on input parameter uncertainty. The total energy metric comparison between the model and the experiment illustrated an increased percent difference relative to the curvature comparison. This increased discrepancy is attributed to the increased dependency on the input parameters in the model energy equation, Eq. (3), via three active terms (ε_o, κ, and ε_m), and thus increased uncertainty in the model derived ratio. However, the energy result was consistent and contained within the range of expected values, accounting for model parameter uncertainty, and thus aligned with the model curvature to experimental elastic strain gradient comparison, to support the effect of coating crystallinity on the residual elastic strain state.

Overall, the agreement between these experimental strain metrics and the model results justified that the difference in residual elastic strain state between the tetragonal SmSZ-Dep coating and the cubic YSZ-Dep coating was a consequence of the tetragonality ($c/a = 1.0013$) of the SmSZ coating and the corresponding difference in elastic and thermal properties. The comparison between the model curvature ratio (Θ) to the experimental elastic strain gradient ratio (β) as well as the model potential energy ratio (Φ) to the experimental total elastic strain energy ratio (Ψ) were both individually congruent when accounting for input uncertainty. Furthermore, the trend in the reduction in the magnitude of the ratios from the gradient comparison to the energy comparison was consistent between both the model and experimental results. This agreement illustrated the value of a fundamental analytical model to understand the residual stress trends in plasma-sprayed ceramic coatings.

5. Conclusions

In this work, the residual elastic strain state of two varieties of plasma-sprayed stabilized zirconia-based coatings, 12 mol% yttria (YSZ) and 6 mol% samaria (SmSZ), applied to C/C was quantified via high energy X-ray EDD. The benefits of the high flux synchrotron experimental setup included (i) bulk measurements of samples large enough to reduce surface and edge effects on the stress state, (ii) relaxation of the assumptions necessary for $\sin^2\psi$ thin film residual stress analysis, and (iii) multiple strain measurements from distinct lattice planes in a single scan to reduce experimental uncertainty via the weighted average metric and to homogenize the diffraction-based measurement for comparison to isotropic model formulations. These advantages in combination with the fine depth-resolution and strain fidelity in the experimental results showed that cooling from deposition resulted in a tension to compression gradient (−1.17e−3 and −8.79e−4 percent strain per micron for YSZ and for SmSZ, respectively) of in-plane residual elastic strain in both zirconia-based coatings applied to C/C. Furthermore, the experimentally identified variations in elastic strain state between the cubic YSZ and the tetragonal SmSZ coating were correlated to a finite thickness coating model via a comparison of both (i) the model-derived curvature ($\Theta^* = 0.78$) values to the experimentally measured elastic strain gradients ($\beta = 0.75$) and (ii) the model-derived potential energy ($\Phi^* = 0.66$) values to the experientially measured elastic strain energy densities ($\Psi = 0.52$). The model was consistent with the experimental results in both metrics to support the crystal structure dependence of the residual stress state in these plasma sprayed zirconia coatings. Finally, via oxyacetylene torch exposure testing of a YSZ coated sample, the ablation behavior and crack failure mechanisms were studied. The strain measurements were compared to microscopy results of the torch-exposed sample and were consistent with crack arrestment and improved coating survivability due to residual compressive strain of approximately −0.1 percent strain near the coating-substrate interface. Also, the 60 μm depth of ablation correlated well to the depth of the residual tensile strain from deposition, which indicated the impact of processing-induced residual stress on coating performance in application.

From these findings, plasma-sprayed stabilized-zirconia coatings are shown to be candidate materials for protection of C/C in high-temperature applications. Specifically, the YSZ/SiC coating proved survivability and sustained protection in an oxidizing high temperature environment and the SmSZ/SiC coating is expected to perform comparably based upon the similarities in residual stress state and proven thermal stability, with the benefit of improved emissivity. In addition to these validations of the specific coating systems, this work showed the importance of zirconia coating crystal structure on the residual stress state, as well as more broadly the direct effects of post-deposition residual stress on ablation behavior, crack propagation, and ultimately coating survivability. Furthermore, the residual elastic strain profiles found in this work can be instantiated and applied in future models to design components with ceramic oxidation protection coatings applied to C/C substrates to serve as thermal protection systems, while the finite thickness coating analytical model can be a valuable fundamental tool

for comprehending experimental residual elastic strain results. Future work is needed to understand the stress state of the SiC intermediate layer and the substrate C/C to inform potential interfacial failure, spallation, and exfoliation.

CRediT authorship contribution statement

John I. Ferguson: Conceptualization, Data curation, Formal analysis, Investigation, Software, Validation, Visualization, Writing – original draft. **Abdullah Al Saad:** Data curation, Formal analysis, Investigation, Validation, Visualization, Writing – review & editing. **M. Hazar Seren:** Data curation, Formal analysis, Investigation, Software, Validation, Writing – review & editing. **J.Y. Peter Ko:** Data curation, Investigation, Validation, Writing – review & editing. **Kelly E. Nygren:** Data curation, Investigation, Validation, Writing – review & editing. **Rodney W. Trice:** Conceptualization, Funding acquisition, Investigation, Methodology, Project administration, Resources, Supervision, Validation, Writing – review & editing. **Michael D. Sangid:** Conceptualization, Data curation, Formal analysis, Funding acquisition, Investigation, Methodology, Project administration, Resources, Supervision, Validation, Visualization, Writing – review & editing.

Declaration of competing interest

The authors declare that they have no known competing financial interests or personal relationships that could have appeared to influence the work reported in this paper.

Data availability

Data will be made available on request.

Acknowledgements

MDS would like to thank the National Science Foundation [grant number CMMI 16-5196] for financial support. RWT would like to thank the Office of Naval Research [grant number N00014-20-1-2262]. This work is based upon research conducted at the Center for High Energy X-ray Sciences (CHEXS) which is supported by the National Science Foundation (BIO, ENG and MPS Directorates) under award DMR-1829070, and at the Materials Solutions Network at CHESS (MSN-C) which is supported by the Air Force Research Laboratory under award FA8650-19-2-5220.

References

[1] T. Windhorst, G. Blount, Carbon-carbon composites: a summary of recent developments and applications, Mater. Des. 18 (1997) 11–15, https://doi.org/10.1016/S0261-3069(97)00024-1.
[2] E. Fitzer, The future of carbon-carbon composites, Carbon N.Y. 25 (1987) 163–190, https://doi.org/10.1016/0008-6223(87)90116-3.
[3] J. Neumeister, S. Jansson, F. Leckie, The effect of fiber architecture on the mechanical properties of carbon/carbon fiber composites, Acta Mater 44 (1996) 573–585, https://doi.org/10.1016/1359-6454(95)00184-0.
[4] D.W. Mckee, Oxidation behavior and protection of carbon/carbon composites, Carbon N.Y. 25 (1987) 551–557, https://doi.org/10.1016/0008-6223(87)90197-7.
[5] W.L. Luthra, Oxidation of carbon-carbon composites - a theoretical analysis, Carbon N.Y. 26 (1988) 217–224, https://doi.org/10.1016/0008-6223(88)90040-1.
[6] S.D. Williams, D.M. Curry, D.C. Chao, V.T. Pham, Ablation analysis of the shuttle orbiter oxidation protected reinforced carbon-carbon, J Thermophys Heat Trans, American Institute of Aeronautics and Astronautics Inc. (1995) 478–485, https://doi.org/10.2514/3.690.
[7] Q.G. Fu, H.J. Li, X.H. Shi, K.Z. Li, G.D. Sun, Silicon carbide coating to protect carbon/carbon composites against oxidation, Scr. Mater. 52 (2005) 923–927, https://doi.org/10.1016/j.scriptamat.2004.12.029.
[8] H. Fritze, J. Jojic, T. Witke, C. Rüscher, S. Weber, S. Scherrer, R. Weiß, B. Schultrich, G. Borchardt, Mullite based oxidation protection for SiC-C/C composites in air at temperatures up to 1900 K, J. Eur. Ceram. Soc. 18 (1998) 2351–2364, https://doi.org/10.1016/S0955-2219(98)00242-8.
[9] C.A.A. Cairo, M.L.A. Graça, C.R.M. Silva, J.C. Bressiani, Functionally gradient ceramic coating for carbon-carbon antioxidation protection, J. Eur. Ceram. Soc. 21 (2001) 325–329, https://doi.org/10.1016/S0955-2219(00)00191-6.
[10] Q. Zhen, Z. Li, P. Hu, S. Song, F. Zheng, A glass-ceramic coating with self-healing capability and high infrared emissivity for carbon/carbon composites, Corros. Sci. 141 (2018) 81–87, https://doi.org/10.1016/j.corsci.2018.06.041.
[11] C. Wang, K. Li, X. Shi, J. Sun, Q. He, C. Huo, Self-healing YSZ-La-Mo-Si heterogeneous coating fabricated by plasma spraying to protect carbon/carbon composites from oxidation, Compos. B Eng. 125 (2017) 181–194, https://doi.org/10.1016/j.compositesb.2017.05.078.
[12] Y. Zeng, X. Xiong, S. Guo, W. Zhuang Zhang, SiC/SiC-YAG-YSZ oxidation protective coatings for carbon/carbon composites, Corros. Sci. 70 (2013) 68–73, https://doi.org/10.1016/j.corsci.2013.01.013.
[13] Y. Xu, X. Hu, F. Xu, K. Li, Rare earth silicate environmental barrier coatings: present status and prospective, Ceram. Int. 43 (2017) 5847–5855, https://doi.org/10.1016/j.ceramint.2017.01.153.
[14] K. Knipe, A. Manero, S.F. Siddiqui, C. Meid, J. Wischek, J. Okasinski, J. Almer, A. M. Karlsson, M. Bartsch, S. Raghavan, Strain response of thermal barrier coatings captured under extreme engine environments through synchrotron X-ray diffraction, Nat. Commun. 5 (2014), https://doi.org/10.1038/ncomms5559.
[15] R. Diaz, M. Jansz, M. Mossaddad, S. Raghavan, J. Okasinski, J. Almer, H. Pelaez-Perez, P. Imbrie, Role of mechanical loads in inducing in-cycle tensile stress in thermally grown oxide, Appl. Phys. Lett. 100 (2012), https://doi.org/10.1063/1.3692592.
[16] C. Li, S.D.M. Jacques, Y. Chen, P. Xiao, A.M. Beale, M. Di Michiel, N. Markossan, P. Nylen, R.J. Cernik, Precise strain profile measurement as a function of depth in thermal barrier coatings using high energy synchrotron X-rays, Scr. Mater. 113 (2016) 122–126, https://doi.org/10.1016/j.scriptamat.2015.10.032.
[17] S. Sampath, X.Y. Jiang, J. Matejicek, L. Prchlik, A. Kulkarni, A. Vaidya, Role of thermal spray processing method on the microstructure, residual stress and properties of coatings: an integrated study of Ni-5 wt. % Al bond coats, Mater. Sci. Eng. A 364 (2004) 216–231, https://doi.org/10.1016/j.msea.2003.08.023.
[18] V. Teixeira, Numerical analysis of the influence of coating porosity and substrate elastic properties on the residual stresses in high temperature graded coatings, Surf. Coat. Technol. 146-147 (2001) 79–84, https://doi.org/10.1016/S0257-8972(01)01457-8.
[19] J.D. Lee, H.Y. Ra, K.T. Hong, S.K. Hur, Analysis of deposition phenomena and residual stress in plasma spray coatings, Surf. Coat. Technol. 56 (1992) 27–37, https://doi.org/10.1016/0257-8972(92)90192-D.
[20] S. Kuroda, T. Dendo, S. Kitahara, Quenching stress in plasma sprayed coatings and its correlation with the deposit microstructure, J. Therm. Spray Technol. 4 (1995) 75–84, https://doi.org/10.1007/BF02648531.
[21] A. Al Saad, C. Martinez, R.W. Trice, Ablation performance of rare earth oxide (REO)-stabilized tetragonal and cubic zirconia coatings as thermal protection system (TPS) for carbon/carbon composites, J. Eur. Ceram. Soc. 43 (2023), https://doi.org/10.1016/j.jeurceramsoc.2023.06.028.
[22] J.P. Zhang, Q.G. Fu, J.L. Qu, H.J. Li, Pre-ablation treatment of carbon/carbon composites to improve the thermal shock resistance for SiC coating under oxyacetylene torch, Appl. Surf. Sci. 355 (2015) 638–643, https://doi.org/10.1016/j.apsusc.2015.07.161.
[23] J. Hao, J. Li, W. Shi, B. Wang, Y. Tan, The novel effect mechanism of Al_2O_3 nano-powder in the pack cementation process to prepare SiC coating on C/C composites, J. Eur. Ceram. Soc. 41 (2021) 1107–1113, https://doi.org/10.1016/j.jeurceramsoc.2020.10.014.
[24] R. Vassen, A. Stuke, D. Stöver, Recent developments in the field of thermal barrier coatings, J. Therm. Spray Technol. 18 (2009) 181–186, https://doi.org/10.1007/s11666-009-9312-7.
[25] Y. Shao, Y. Yang, C. Zhao, W. Tian, Phase transitions and microstructure evolutions of in-situ YSZ-ZrC composite coating under long-time plasma torch ablation, Surf. Coat. Technol. 466 (2023), 129636, https://doi.org/10.1016/j.surfcoat.2023.129636.
[26] W. Tan, C.A. Petorak, R.W. Trice, Rare-earth modified zirconium diboride high emissivity coatings for hypersonic applications, J. Eur. Ceram. Soc. 34 (2014) 1–11, https://doi.org/10.1016/j.jeurceramsoc.2013.07.016.
[27] A. Al Saad, C. Martinez, R.W. Trice, Radiation heat transfer during hypersonic flight: a review of emissivity measurement and enhancement approaches of ultra-high temperature ceramics, Int. J. Ceram. Eng. Sci. (2023), https://doi.org/10.1002/ces2.10171.
[28] W. Tan, M. Adducci, C. Petorak, B. Thompson, A.E. Brenner, R.W. Trice, Effect of rare-earth dopant (Sm) concentration on total hemispherical emissivity and ablation resistance of ZrB2/SiC coatings, J. Eur. Ceram. Soc. 36 (2016) 3833–3841, https://doi.org/10.1016/j.jeurceramsoc.2016.04.013.
[29] M. Vardelle, A. Vardelle, P. Fauchais, Spray parameters and particle behavior relationships during plasma spraying, J. Therm. Spray Technol. 2 (1993) 79–92, https://doi.org/10.1007/BF02647426.
[30] G. Mauer, R. Vaßen, D. Stöver, Plasma and particle temperature measurements in thermal spray: approaches and applications, J. Therm. Spray Technol. 20 (2011) 391–406, https://doi.org/10.1007/s11666-010-9603-z.
[31] Y.B. Guo, A.W. Warren, F. Hashimoto, The basic relationships between residual stress, white layer, and fatigue life of hard turned and ground surfaces in rolling contact, CIRP J. Manuf. Sci. Technol. 2 (2010) 129–134, https://doi.org/10.1016/j.cirpj.2009.12.002.
[32] J.I. Ferguson, A.J. Beaudoin, G.D. Scofield, J.Y.P. Ko, K.E. Nygren, Y. Wang, M. Caccia, K.H. Sandhage, M.D. Sangid, Residual elastic strain evolution due to thermal cycling of a ceramic-metal composite (WC-Cu) via high energy X-ray diffraction and analytical modeling, Int. J. Refract. Met. Hard Mater. 110 (2023), https://doi.org/10.1016/j.ijrmhm.2022.106018.
[33] P. Virtanen, R. Gommers, T.E. Oliphant, M. Haberland, T. Reddy, D. Cournapeau, E. Burovski, P. Peterson, W. Weckesser, J. Bright, S.J. van der Walt, M. Brett,

J. Wilson, K.J. Millman, N. Mayorov, A.R.J. Nelson, E. Jones, R. Kern, E. Larson, C. J. Carey, İ. Polat, Y. Feng, E.W. Moore, J. VanderPlas, D. Laxalde, J. Perktold, R. Cimrman, I. Henriksen, E.A. Quintero, C.R. Harris, A.M. Archibald, A.H. Ribeiro, F. Pedregosa, P. van Mulbregt, A. Vijaykumar, A. Pietro Bardelli, A. Rothberg, A. Hilboll, A. Kloeckner, A. Scopatz, A. Lee, A. Rokem, C.N. Woods, C. Fulton, C. Masson, C. Häggström, C. Fitzgerald, D.A. Nicholson, D.R. Hagen, D. v Pasechnik, E. Olivetti, E. Martin, E. Wieser, F. Silva, F. Lenders, F. Wilhelm, G. Young, G.A. Price, G.L. Ingold, G.E. Allen, G.R. Lee, H. Audren, I. Probst, J. P. Dietrich, J. Silterra, J.T. Webber, J. Slavič, J. Nothman, J. Buchner, J. Kulick, J. L. Schönberger, J.V. de Miranda Cardoso, J. Reimer, J. Harrington, J.L. C. Rodríguez, J. Nunez-Iglesias, J. Kuczynski, K. Tritz, M. Thoma, M. Newville, M. Kümmerer, M. Bolingbroke, M. Tartre, M. Pak, N.J. Smith, N. Nowaczyk, N. Shebanov, O. Pavlyk, P.A. Brodtkorb, P. Lee, R.T. McGibbon, R. Feldbauer, S. Lewis, S. Tygier, S. Sievert, S. Vigna, S. Peterson, S. More, T. Pudlik, T. Oshima, T.J. Pingel, T.P. Robitaille, T. Spura, T.R. Jones, T. Cera, T. Leslie, T. Zito, T. Krauss, U. Upadhyay, Y.O. Halchenko, Y. Vázquez-Baeza, SciPy 1.0: fundamental algorithms for scientific computing in Python, Nat. Methods 17 (2020) 261–272, https://doi.org/10.1038/s41592-019-0686-2.

[34] D.E. Boyce, J.V. Bernier, heXRD: Modular, open source software for the analysis of high energy X-ray diffraction data, Lawrence Livermore National Lab (LLNL), Livermore, CA (United States), 2013, https://doi.org/10.2172/1062217.

[35] C. Genzel, I.A. Denks, J. Gibmeier, M. Klaus, G. Wagener, The materials science synchrotron beamline EDDI for energy-dispersive diffraction analysis, Nucl. Instrum. Methods Phys. Res. A 578 (2007) 23–33, https://doi.org/10.1016/j.nima.2007.05.209.

[36] G.G. Stoney, The tension of metallic films deposited by electrolysis, Proc. R. Soc. Lond. Ser. A 82 (1909) 172–175, https://doi.org/10.1098/rspa.1909.0021.

[37] L.B. Freund, J.A. Floro, E. Chason, Extensions of the Stoney formula for substrate curvature to configurations with thin substrates or large deformations, Appl. Phys. Lett. 74 (1999) 1987–1989, https://doi.org/10.1063/1.123722.

[38] L.B. Freund, S. Suresh, Thin Film Materials Stress, Defect Formation and Surface Evolution, Cambridge University Press, 2010, https://doi.org/10.1017/cbo9780511754715.003.

[39] R. Saeidpourazar, M.D. Sangid, J.A. Rogers, P.M. Ferreira, A prototype printer for laser driven micro-transfer printing, J. Manuf. Process. 14 (2012) 416–424, https://doi.org/10.1016/j.jmapro.2012.09.014.

[40] D.J. Johnson, Structure-property relationships in carbon fibres, J. Phys. D. Appl. Phys. 20 (1987) 286–291, https://doi.org/10.1088/0022-3727/20/3/007.

[41] I. Krucinska, T. Stypka, Direct measurement of the axial Poisson's ratio of single carbon fibres, Compos. Sci. Technol. 41 (1991) 1–12, https://doi.org/10.1016/0266-3538(91)90049-U.

[42] J.G. Zhao, K.Z. Li, H.J. Li, C. Wang, Y.Q. Zhai, The thermal expansion of carbon/carbon composites from room temperature to 1400 °C, J. Mater. Sci. 41 (2006) 8356–8358, https://doi.org/10.1007/s10853-006-1073-9.

[43] J. Sure, K. Thyagarajan, C. Mallika, U.K. Mudali, Thermal-cycling behavior of plasma-sprayed partially stabilized zirconia coatings on high-density graphite substrate, J. Therm. Spray Technol. 24 (2015) 925–937, https://doi.org/10.1007/s11666-015-0268-5.

[44] N. Song, Z. Wang, Y. Xing, M. Zhang, P. Wu, F. Qian, J. Feng, L. Qi, C. Wan, W. Pan, Evaluation of phase transformation and mechanical properties of metastable yttria-stabilized zirconia by nanoindentation, Materials. 12 (2019), https://doi.org/10.3390/MA12101677.

[45] G.P. Cousland, X.Y. Cui, A.E. Smith, A.P.J. Stampfl, C.M. Stampfl, Mechanical properties of zirconia, doped and undoped yttria-stabilized cubic zirconia from first-principles, J. Phys. Chem. Solids 122 (2018) 51–71, https://doi.org/10.1016/j.jpcs.2018.06.003.

[46] J.W. Adams, H.H. Nakamura, R.P. Ingel, R.W. Rice, Thermal expansion behavior of single-crystal zirconia, J. Am. Ceram. Soc. 68 (1985) 228–231, https://doi.org/10.1111/j.1151-2916.1985.tb15793.x.

[47] S. Giraud, J. Canel, Young's modulus of some SOFCs materials as a function of temperature, J. Eur. Ceram. Soc. 28 (2008) 77–83, https://doi.org/10.1016/j.jeurceramsoc.2007.05.009.

[48] F.J. Ritzert, H.M. Yun, R.V. Miner, Single crystal fibers of yttria-stabilized cubic zirconia with ternary oxide additions, J. Mater. Sci. 33 (1998) 5339–5349, https://doi.org/10.1023/A:1004438031140.

[49] K. Ma, J. Zhu, H. Xie, H. Wang, Effect of porous microstructure on the elastic modulus of plasma-sprayed thermal barrier coatings: experiment and numerical analysis, Surf. Coat. Technol. 235 (2013) 589–595, https://doi.org/10.1016/j.surfcoat.2013.08.030.

[50] J.S. Wallace, J. Ilavsky, Elastic modulus measurements in plasma sprayed deposits, J. Therm. Spray Technol. 7 (1998) 521–526, https://doi.org/10.1361/105996398770350747.

[51] A. Kucuk, C.C. Berndt, U. Senturk, R.S. Lima, C.R.C. Lima, Influence of plasma spray parameters on mechanical properties of yttria stabilized zirconia coating. I: four point bend test, Mater. Sci. Eng. A 284 (2000) 29–40, https://doi.org/10.1016/S0921-5093(00)00799-1.

[52] X. Zhang, M. Watanabe, S. Kuroda, Effects of residual stress on the mechanical properties of plasma-sprayed thermal barrier coatings, Eng. Fract. Mech. 110 (2013) 314–327, https://doi.org/10.1016/j.engfracmech.2013.08.016.

[53] R. Kromer, Y. Danlos, E. Aubignat, C. Verdy, S. Costil, Coating deposition and adhesion enhancements by laser surface texturing—metallic particles on different classes of substrates in cold spraying process, Mater. Manuf. Process. 32 (2017) 1642–1652, https://doi.org/10.1080/10426914.2017.1364750.

[54] J.G. Odhiambo, W.G. Li, Y.T. Zhao, C.L. Li, Porosity and its significance in plasma-sprayed coatings, Coatings. 9 (2019), https://doi.org/10.3390/coatings9070460.

[55] R. Vaßen, F. Traeger, D. Stöver, Correlation between spraying conditions and microcrack density and their influence on thermal cycling life of thermal barrier coatings, J. Therm. Spray Technol. 13 (2004) 396–404, https://doi.org/10.1361/10599630420443.

[56] J.R. Brandon, R. Taylor, Phase stability of zirconia-based thermal barrier coatings part I. Zirconia-yttria alloys, Surf. Coat. Technol. 46 (1991) 75–90, https://doi.org/10.1016/0257-8972(91)90151-L.

[57] P.F. Gardner, S.J. Noone, R. Bandyopadhyay, J.S. Park, K. Walker, M.D. Sangid, Damage tolerance assessment of laser clad repairs of coarse grain Ti-6Al-4V, Exp. Mech. 62 (2022) 1421–1436, https://doi.org/10.1007/s11340-022-00846-6.

[58] P.J. Withers, M.R. Daymond, M.W. Johnson, The precision of diffraction peak location, J. Appl. Crystallogr. 34 (2001) 737–743, https://doi.org/10.1107/S002188980101411X.